

Frequency Stability-Constrained Unit Commitment: Tight Approximation using Bernstein Polynomials

Bo Zhou, *Member, IEEE*, Ruiwei Jiang, *Member, IEEE*, and Siqian Shen

Abstract—As we replace conventional synchronous generators with renewable energy, the frequency security of power systems is at higher risk. This calls for a more careful consideration of unit commitment (UC) and primary frequency response (PFR) reserves. This paper studies frequency stability-constrained UC under significant wind power uncertainty. We coordinate the thermal units and wind farms to provide frequency support, wherein we optimize the variable inverter droop factors of the wind farms for cost minimization. In addition, we adopt distributionally robust chance constraints (DRCCs) to handle the wind power uncertainty. To depict the frequency dynamics, we incorporate a differential-algebraic equation (DAE) with dead band into the UC model. Notably, we apply Bernstein polynomials to derive tight inner approximation of the DAE and drive a mixed-integer linear representation, which can be solved by off-the-shelf solvers. Case studies demonstrate the tightness and effectiveness of the proposed method in guaranteeing frequency security.

Index Terms—Unit commitment, frequency security, differential-algebraic equation, Bernstein polynomial, variable droop factors, distributionally robust chance constraint

I. INTRODUCTION

A. Background

THE energy and climate crisis has motivated sustainable development and an explosive increase of renewable energy use worldwide [1]. However, the significant integration of renewables brings up many challenges. Among them, frequency security has drawn increasing attention [2]. Different from synchronous thermal units that have rotors and governors, renewable generation is usually controlled by inverters, which cannot provide rotational inertia and primary frequency response (PFR) under the typical maximum power point tracking mode [3]. As renewables gradually replace thermal units, the total rotational inertia and PFR capacity in the power system decrease. Consequently, when a sudden power imbalance occurs, the system frequency will change more sharply and deviate from the nominal frequency more drastically, threatening the frequency security.

A significant amount of effort has been devoted to ensuring frequency security under a high renewable penetration. Straightforwardly, one can keep sufficient synchronous units online, yet this may induce large curtailment of renewables. Some prior studies considered emergency resources for frequency support, such as energy storage [4] and HVDC links [5]. Especially, modern energy storage, such as flywheel

[6] and battery [7], plays an important role in supporting frequency stability of renewable-integrated power systems. However, these approaches incur either high investment cost or operational risks. Fortunately, modern development of control technologies has allowed renewables themselves to contribute to frequency support [8]. Using proper control strategies, renewables can adjust their integrated power according to frequency deviation and provide virtual inertia and PFR capacity [9]. This is relatively cheaper and more practical as the integration of renewables further increases. As a result, renewable generation is becoming an important resource that can be coordinated with thermal units to guarantee frequency security.

Nevertheless, providing frequency support changes operations in power systems. On the one hand, sufficient inertia is required to depress sharp frequency variations, and hence, more units may need to be put online [10], [11]. On the other hand, sufficient PFR reserves are required for effective real-time PFR, for which thermal units need to reserve some generation capacity [12] and renewable generation will be operated under the deloaded mode [13]. Both of the required changes will increase the operational cost, yet they are coupled to influence frequency dynamics and further affect frequency security. Therefore, it is of great significance to carefully decide unit commitment (UC) and PFR reserves, in order to maintain frequency security in an economic manner.

B. Literature Review

A significant amount of literature has considered frequency security in scheduling, such as economic dispatch [14], UC [15], and energy market [16]. However, due to the complex coupling of frequency dynamics, various frequency support resources, and the uncertainty of renewables, it remains extremely challenging to compute frequency stability-constrained UC accurately and tractably, which is the research focus of this paper. In the following, we conduct the literature review from two aspects, modeling frequency security constraints and handling uncertainties for frequency security.

Three metrics of frequency dynamics are often considered, including the rate of change of frequency (RoCoF), the frequency nadir, and the quasi-steady-state (QSS) frequency deviation [17]. However, these metrics are difficult to calculate because frequency dynamics are governed by a series of differential-algebraic equations (DAEs) [18]. Additionally, complex control process, such as the dead band that is utilized to avoid frequent PFR and to reduce the maintenance cost of governors, needs to be considered yet further complicates the computation [19]. Much effort has been devoted to simulating or approximating frequency dynamics and TABLE I

Ruiwei Jiang was supported in part by the U.S. National Science Foundation under Grant ECCS-1845980. Bo Zhou and Siqian Shen were supported in part by the U.S. Department of Energy, Grant #DE-SC0018018. (Corresponding author: Bo Zhou, email: bozum@umich.edu)

The authors are with the Department of Industrial and Operations Engineering, University of Michigan, Ann Arbor, MI 48109, USA.

TABLE I
COMPARISON OF MAIN METHODS FOR CALCULATING THE FREQUENCY NADIR

Method		Response dynamics	Different response constants	Dead band	Encoding nadir constraints	Reference
Numerical simulation		Yes	Yes	Yes	N/A	MATLAB/Simulink
Neural network prediction		Yes	Yes	Yes	Mixed-integer linearization	[36], [37]
Linear ramping model		No	Yes	Yes	Sufficient condition	[30]–[35]
Dynamic response model	Analytical expression	Yes	No	No	Piecewise linearization	[20]–[25]
					Inner approximation	[26], [27]
	DAE constraints	Yes	Yes	Yes	Difference method	[28], [29]
					Our method	–

provides a review and comparison of existing methods and ours. Numerical simulation tools (such as Simulink), which are commonly utilized in transient analysis, can encode complex control strategies and thus accurately evaluate frequency dynamics. Nonetheless, these methods are computationally heavy and intractable to compute in optimization models. For frequency stability-constrained optimization, existing approaches are mainly based on the system frequency response (SFR) model, which have been extended in various ways. The first variant is dynamic response models, which consider the frequency dynamics [20]–[29]. The difference method is a straightforward method to handle the DAEs of the model [28], [29], in which small time steps are required for accurate modeling but it incurs a heavy computational burden. Most works on dynamic response models assume the response time of different PFR resources to be the same and ignore the dead band, through which frequency dynamics and its nadir can be analytically derived. Yet, these assumptions are less practical and the derived analytical expression of nadir is highly nonlinear, for which complex approximation methods are further required to handle the intractability, such as piecewise linearization [20]–[25] and inner approximations [26], [27]. Second, some studies simplify the dynamic response model by assuming a linear ramping for PFR, wherein the dead band can be embedded [30]–[35]. But such simplification ignores PFR dynamics and induces low accuracy. Moreover, the approach also results in nonlinear expressions for frequency nadir constraints, and consequently, sufficient conditions are adopted for tractable calculation [30]–[35], most of which are unfortunately conservative and sacrifice the economy. Finally, other variants consider machine learning techniques and utilize neural networks to fit the nonlinear frequency dynamics [36], [37]. With proper sampling and training, such neural network-based methods can capture the dynamic characteristics to yield an accurate prediction of frequency dynamics. Nevertheless, few have considered the dead band and the neural network is computationally prohibitive to use in optimization models. In this paper, we aim to model frequency security constraints that incorporate both frequency dynamics and the dead band into UC in a tractable manner.

Renewable generation is uncertain, which strongly impacts PFR capacities and frequency dynamics. In what follows, we consider wind power as an example [38] and the same approach adapts to other renewables. Due to wind uncertainties, the real-time available wind generation may be different from the day-ahead forecast that is used to decide the PFR

reserves of wind farms. If the available wind generation is less than the required PFR reserves, PFR capacities from wind farms will be limited, resulting in a larger frequency deviation and threatening frequency security [12], [13]. Two approaches have been studied to address this issue. First, the frequency stability-constrained UC model explicitly incorporates wind uncertainties using, e.g., stochastic approximation [21], chance constraints [30], [31], [39]–[41], and robust optimization [42], [43]. In this paper, we adopt distributionally robust chance constraints (DRCCs) in view of their tractability and good out-of-sample performance [44]–[46]. Second, we adjust PFR reserves across time, e.g., through the droop factors used in the control strategy of wind farm inverters [47], in response to varying wind generation. We note that the droop factors in [47] are predefined device parameters, which vary for different frequency deviation but remain constant across time. In contrast, we consider droop factors as decision variables and optimize their values over time. Variable droop factors also help to better coordinate thermal units and wind farms in providing frequency support and enhancing the operational economy. Therefore, both DRCCs and variable droop factors are considered in this work to better accommodate wind uncertainties.

C. Contributions and Paper Organization

Considering the time-domain characteristic of frequency dynamics, Bernstein polynomials (BPs) are promising to handle the above research gaps due to their tractability for continuous-time optimization [48], which has shown superiority in exploiting flexibility [49], [50] and modeling natural gas transmission [51]. This paper proposes a tight, Bernstein polynomials (BPs)-based approximation method for frequency stability-constrained UC, which enables UC to incorporate more details of frequency dynamics (e.g., different response constants, the dead band and variable droop factors) while keeping the model tractability. Our main contributions are summarized as follows.

- 1) We propose a frequency stability-constrained UC model to accommodate under-frequency events, which incorporates time-domain frequency dynamics, different response constants, the dead band control, and variable droop factors. Thermal units and wind farms are coordinated to provide frequency support.
- 2) We develop a tight, BP-based approximation to transform time-domain frequency security constraints, which involve intractable DAEs, into mixed-integer linear constraints that can be computed by off-the-shelf solvers.

3) Through extensive case studies, we demonstrate the tightness of the BP approximation, the necessity of considering the dead band, the value of using variable droop factors, and the scalability of our approach.

The remainder of this paper is organized as follows. Section II establishes the problem formulation of frequency stability-constrained UC under wind power uncertainty. Section III derives the BP approximation of frequency dynamics DAEs and a tractable reformulation of the DRCCs. Case studies are conducted in Section IV and conclusions are drawn in Section V.

II. PROBLEM FORMULATION

We first introduce the general process of frequency dynamics, then propose the DAE frequency security constraints, and finally formulate a frequency stability-constrained UC model.

A. Frequency Dynamics

Fig. 1 depicts a general process of frequency dynamics under a sudden loss of generation at time t_0 . At the beginning (time t_0-t_{DB}), before the frequency deviation exceeds the dead band Δf_{DB} , the governors do not work and inertia plays the whole role in mitigating the frequency drop. Generally, the maximum RoCoF occurs at t_0 . As the frequency deviation exceeds Δf_{DB} , the governors start working, and PFR becomes significant (time $t_{DB}-t_{QSS}$), the frequency eventually reaches a QSS with deviation Δf_{QSS} . During the whole dynamics, frequency first drops and is then lifted, yielding a nadir with deviation Δf_{nadir} at t_{nadir} .

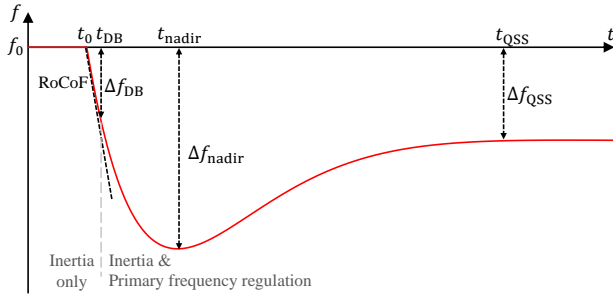


Fig. 1. A general process of the frequency dynamics

B. DAE Frequency Security Constraints

We depict the SFR model [18] of frequency dynamics in Fig. 2. We note that the paper uses the center of inertia (COI) assumption, which calculates average frequency and ignores local frequency dynamics. In this model, ΔP_d is the power imbalance, $\Delta f(t) = f_0 - f(t)$ is the frequency deviation from the nominal frequency f_0 at time instant t , P_{sys}^{PR} is the total PFR power in the power system, and P_g^{PR} and P_w^{PR} are the PFR power from thermal units and wind farms, respectively. To avoid frequent PFR, the governors of thermal units and inverters of wind farms will not respond to a non-zero $\Delta f(t)$ unless its magnitude exceeds the dead band Δf_{DB} .

This divides the frequency dynamics into two stages. In the first stage, frequency deviation lies within the dead band and

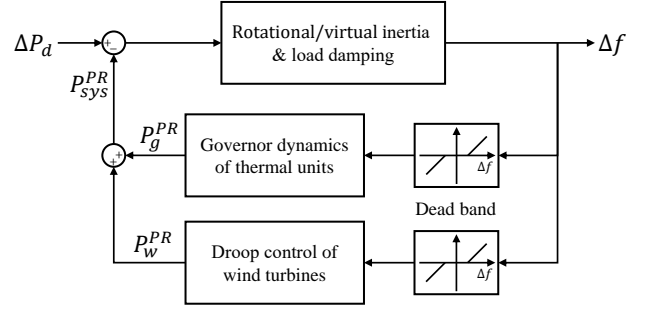


Fig. 2. SFR model considering the dead band

thus there is no PFR. As in Fig. 2, system frequency dynamics follow the governing equations

$$2H_{sys} \frac{d\Delta f(t)}{dt} + k_D P_d \Delta f(t) = \Delta P_d, \quad t \in [0, t_{DB}] \quad (1a)$$

$$\Delta f(t)|_{t=0} = 0, \quad \Delta f(t)|_{t=t_{DB}} = \Delta f_{DB}, \quad (1b)$$

where H_{sys} is the total inertia in the power system, including rotational inertia H_g from thermal units and virtual inertia H_w from wind farms, k_D is the load damping rate, and P_d is the power load. We note that H_w is implemented through the virtual inertia control of wind turbines [52], [53], which is adjustable but is treated as an input parameter in this paper. Constraint (1b) gives the initial and final conditions of the ordinary differential equation (1a). Note that t_{DB} in (1) is not a given parameter, but a variable that depends on frequency dynamics and the dead band Δf_{DB} . In the second stage, frequency deviation exceeds Δf_{DB} and PFR starts working. Accordingly, the system frequency dynamics follow the governing equations

$$2H_{sys} \frac{d\Delta f(t)}{dt} + k_D P_d \Delta f(t) = \Delta P_d - P_{sys}^{PR}(t), \quad t \geq t_{DB} \quad (2a)$$

$$\Delta f(t)|_{t=t_{DB}} = \Delta f_{DB} \quad (2b)$$

$$P_{sys}^{PR}(t) = \sum_i [P_{g,i}^{PR}(t) + P_{w,i}^{PR}(t)] \quad (3a)$$

$$T_{g,i} \frac{dP_{g,i}^{PR}(t)}{dt} + P_{g,i}^{PR}(t) = G_{g,i} I_{g,i} [\Delta f(t) - \Delta f_{DB}] \quad (3b)$$

$$P_{g,i}^{PR}(t)|_{t=t_{DB}} = 0 \quad (3c)$$

$$P_{w,i}^{PR}(t) = G_{w,i} [\Delta f(t) - \Delta f_{DB}], \quad (3d)$$

where i is the bus index, T_g is the response constant of governors, and G_g is the droop factor of thermal units. The response constant of wind power is $T_w \approx 0$ because it is controlled by inverters. G_w is the variable droop factor of wind farms, which can be adjusted to adapt to wind uncertainties and to enhance the coordination of thermal units and wind farms. Constraint (2b) gives the initial condition of the ordinary differential equation (2a). Constraint (3a) implies that the total PFR power $P_{sys}^{PR}(t)$ comes from all power sources, including thermal units and wind farms. According to the response characteristic of the governors, (3b) describes the dynamics of P_g^{PR} , where I_g indicates the online/offline status of thermal units ($I_g = 1$ if online and $I_g = 0$ if offline). Constraint (3c) provides the initial condition of the ordinary differential equation (3b).

Finally, similar to (3b), (3d) describes the dynamics of the wind farm PFR power P_w^{PR} . Note that we consider non-step dead band control in (3b) and (3d), but the step implementation can also be tractably incorporated with slight adaption.

To protect frequency security, we restrict the RoCoF, nadir, and quasi-steady-state deviation as

$$\frac{d\Delta f(t)}{dt} \leq \bar{f} \quad (4a)$$

$$\Delta f(t)|_{\text{nadir}} \leq \overline{\Delta f} \quad (4b)$$

$$\Delta f(t)|_{\text{QSS}} \leq \overline{\Delta f_{err}}, \quad (4c)$$

where \bar{f} is the maximum admitted RoCoF, and $\overline{\Delta f}$ and $\overline{\Delta f_{err}}$ are the maximum admitted frequency deviation at the nadir and QSS, respectively. Note that without loss of generality, only under-frequency events are considered.

C. Frequency Stability-Constrained Chance-Constrained Unit Commitment

We formulate the following frequency stability-constrained UC model with DAEs and DRCCs.

$$\min_{\tau} \sum_i (c_{su,i} U_{g,i,\tau} + c_{sd,i} D_{g,i,\tau} + F_{g,i,\tau} + c_g^{PR} R_{g,i,\tau}^{PR} + c_w^{PR} R_{w,i,\tau}^{PR}) \quad (5)$$

$$\text{s.t. (1)–(4)}$$

$$\begin{cases} F_{g,i,\tau} = c_{on,i} I_{g,i,\tau} + \sum_k \lambda_{g,i,k} p_{g,i,k,\tau} \\ P_{g,i,\tau} = \underline{P}_{g,i} I_{g,i,\tau} + \sum_k p_{g,i,k,\tau} \\ 0 \leq p_{g,i,k,\tau} \leq (\overline{P}_{g,i} - \underline{P}_{g,i}) / N_{pw} \end{cases} \quad (6)$$

$$U_{g,i,\tau} + D_{g,i,\tau} \leq 1 \quad (7a)$$

$$U_{g,i,\tau} - D_{g,i,\tau} = I_{g,i,(\tau+1)} - I_{g,i,\tau} \quad (7b)$$

$$\begin{cases} \sum_{k=\tau+1}^{t+T_{on,i}} I_{g,i,k} \geq T_{on,i} U_{g,i,\tau} \\ \sum_{k=\tau+1}^{t+T_{off,i}} (1 - I_{g,i,k}) \geq T_{off,i} D_{g,i,\tau} \end{cases} \quad (7c)$$

$$H_{\text{sys},\tau} = \sum_i (H_{g,i} I_{g,i,\tau} + H_{w,i}) \quad (8a)$$

$$\underline{G}_{w,i} \leq G_{w,i,\tau} \leq \overline{G}_{w,i} \quad (8b)$$

$$\begin{cases} P_{g,i,\tau}^{PR}(t) \leq R_{g,i,\tau}^{PR} \\ P_{w,i,\tau}^{PR}(t) \leq R_{w,i,\tau}^{PR} \end{cases} \quad (8c)$$

$$P_{g,i} I_{g,i,\tau} \leq P_{g,i,\tau} \leq \overline{P}_{g,i} I_{g,i,\tau} - R_{g,i,\tau}^{PR} \quad (9a)$$

$$\begin{cases} P_{g,i,(\tau+1)} - P_{g,i,\tau} \leq r_{u,i} I_{g,i,\tau} + r_{su,i} U_{g,i,\tau} \\ P_{g,i,\tau} - P_{g,i,(\tau+1)} \leq r_{d,i} I_{g,i,(\tau+1)} + r_{sd,i} D_{g,i,\tau} \end{cases} \quad (9b)$$

$$\sum_i (P_{g,i,\tau} + P_{w,i,\tau}) = \sum_i P_{d,i,\tau} \quad (10)$$

$$-\overline{P}_{l,j} \leq \sum_i S_{ji} (P_{g,i,\tau} + P_{w,i,\tau} - P_{d,i,\tau}) \leq \overline{P}_{l,j} \quad (11)$$

$$\inf_{\mathbb{P} \in \mathcal{D}} \mathbb{P} \left\{ P_{w,i,\tau} + R_{w,i,\tau}^{PR} \leq P_{w,i,\tau}^A \right\} \geq 1 - \varepsilon, \quad (12)$$

where τ is the index for time periods. The objective (5) consists of start-up/shut-down cost, PFR reserve cost, and fuel cost. Binary decision variables U_g and D_g represent the start-up and shut-down actions of thermal units, respectively, and c_{su} and c_{sd} are the corresponding costs. Continuous decision variables R_g^{PR} and R_w^{PR} represent the PFR reserves of thermal units and wind farms, respectively, and c_g^{PR} and c_w^{PR} are the corresponding unit costs.

Constraints (6) formulate the fuel cost F_g of thermal units as a piecewise linear function of the amount P_g of power generation [54]. Specifically, p_g is the generation segment, N_{pw} is the piecewise number, $\lambda_{g,k}$ is the cost incremental coefficient of the k th segment, and \overline{P}_g and \underline{P}_g are the maximum and minimum power generation of thermal units, respectively. Constraints (7) formulate the UC restrictions, where T_{on} and T_{off} are minimum up and down time, respectively. Constraints (7a)–(7b) formulate the logic among decision variables U_g , D_g , and I_g , and constraints (7c) formulate the minimum up/down time restrictions. Constraints (8) formulate the frequency security, where $\overline{G}_{w,i}$ and $\underline{G}_{w,i}$ are the maximum and minimum values of the inverter droop factor, respectively. In particular, (8a) calculates the total inertia of the power system, and (8c) ensures that the PFR power does not exceed the PFR reserve. We note that the energy of inertial response and droop control comes from PFR reserve and the kinetic energy of rotors, respectively, and hence, the inertial response is not limited by (8c). Constraints (9) describe the ramping restrictions, where r_u/r_d is the upward/downward ramping limit and r_{su}/r_{sd} is the maximum power generation at start-up/shut-down. Constraints (10) describe the system power balance, where P_d is the power load. Constraints (11) describe the line capacity limits, where j is the line index, \overline{P}_l is the line capacity limit, and S_{ji} is the power transfer distribution factor based on DC power flow.

DRCCs (12) ensure the sufficiency of wind power with high probability, where P_w^A and P_w represent the available and integrated power of wind farms, respectively, where $1 - \varepsilon$ is a pre-specified risk threshold. We adopt a Wasserstein ball \mathcal{D} to describe the wind power ambiguity with

$$\mathcal{D} = \{ \mathbb{P} | d_W(\mathbb{P}, \mathbb{P}_N) \leq r \} \quad (13a)$$

$$d_W(\mathbb{P}, \mathbb{P}_N) = \inf_{(\omega, \omega_N) \sim (\mathbb{P}, \mathbb{P}_N)} \mathbb{E}[\| \omega - \omega_N \|], \quad (13b)$$

where \mathbb{P} represents an ambiguous distribution of the wind power, $\mathbb{P}_N = N(\mu_i, \sigma_i^2)$ is the Gaussian distribution with the mean μ and standard deviation σ , and r is the radius of \mathcal{D} . Here, μ equals to the forecast of wind power.

III. SOLUTION ALGORITHM

The proposed formulation (5)–(12) is a mixed-integer non-linear program due to the DAEs and DRCCs. In this section, we recast them as tractable and computable forms. We first derive an inner approximation for DAEs, and then reformulate it as well as the DRCCs as linear constraints.

A. Transformation of Frequency Security Metrics

To handle DAE frequency security constraints, we revisit the three metrics in (4). As analyzed in Section II.A, since the maximum RoCoF occurs at $t = 0$, constraint (4a) is equivalent to

$$2\bar{f}H_{\text{sys},\tau} \geq \Delta P_{d,\tau}. \quad (14)$$

In addition, at the QSS, since $\Delta f(t)$ reaches a steady value, $\Delta f(t)|_{QSS}$ and $P_{(\cdot)}^{PR}(t)$ are unchanging. In other words, both $d\Delta f(t)/dt$ and $dP_{(\cdot)}^{PR}(t)/dt$ equal zero. It follows from (2)–(3) that (4c) is equivalent to

$$k_D P_d \overline{\Delta f_{err}} + G_{\text{sys},\tau} (\overline{\Delta f_{err}} - \Delta f_{DB}) \geq \Delta P_{d,\tau} \quad (15a)$$

$$G_{\text{sys},\tau} = \sum_i (G_{g,i} I_{g,i,\tau} + G_{w,i}), \quad (15b)$$

where G_{sys} represents the sum of droop factors.

Unlike RoCoF and QSS, $\Delta f(t)|_{\text{nadir}}$ is far more challenging to derive. Fortunately, the frequency nadir usually occurs beyond the dead band and so we can focus on the DAEs in (2)–(3). The next subsection derives an inner approximation using BPs.

B. DAE Approximation

We first introduce an approximation framework using BPs and then derive an inner approximation of the DAEs for computation.

1) BP approximation framework:

We restrict the functional form of the variables in the DAEs (2)–(3) using BP splines [48]. Specifically, if we restrict the functional form of a continuous-time function $F(t)$ to be cubic BPs, then

$$F(t) = \sum_{k=0}^3 F^{B,k} B_{3,k}(t) = (F^B)^T B_3(t), \quad t \in [0, 1] \quad (16)$$

where $B_{3,k}(t) := \binom{3}{k} t^k (1-t)^{3-k}$ for all $t \in [0, 1]$ and $k = 0, 1, 2, 3$ is a cubic BP, and $F^B := [F^{B,0}, \dots, F^{B,3}]^T$ are the spline coefficients. This automatically guarantees the differentiability of $F(t)$ and allows us to compute its derivatives and integrals exactly or approximately. In particular,

$$\frac{dF(t)}{dt} = \frac{d(F^B)^T B_3(t)}{dt} = (WF^B)^T B_2(t) \quad (17a)$$

$$\int_0^1 F(t) dt = \mathbf{1}^T F^B / 4 \quad (17b)$$

$$\int_0^t F(t) dt = \int_0^t (F^B)^T B_3(t) dt \approx (F^B)^T L B_3(t), \quad (17c)$$

$$F(t) = 0 \Leftrightarrow (F^B)^T B_3(t) = 0 \Leftrightarrow F^B = 0 \quad (17d)$$

$$F(t) \leq 0 \Leftrightarrow (F^B)^T B_3(t) \leq 0 \Leftrightarrow JF^B \leq 0 \quad (17e)$$

where $B_{2,k}(t)$ represents quadratic BPs, and W [48], L [51], and J [49] are matrices of known entries. It can be seen that through BP approximation, all the derivatives, integrals, equality and inequality constraints of the continuous-time functions can be reformulated as their linear counterparts. We note that, as compared to other spline methods, BPs have some important properties: i) convex–hull property that enables the inequality

transformation (17e), ii) subdivision property that strengthens the inequality transformation (17e), and iii) operation matrices that enable the integral transformation (17c). The interested readers can refer to [48]–[51] for more details.

2) DAE approximation:

We apply the BP approximation framework to derive an inner approximation of the DAEs (2)–(3) and constraint (4b).

First, frequency dynamics are piecewise approximated using BP splines. Fig. 3 depicts an illustrative example. We divide

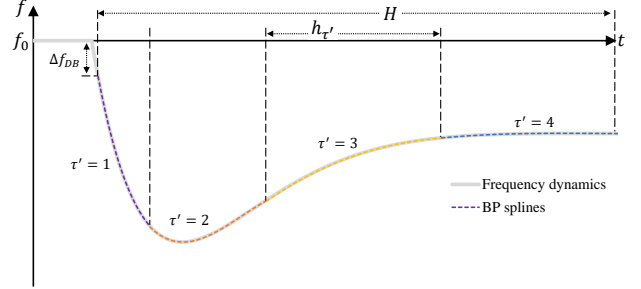


Fig. 3. BP spline-based frequency dynamics

the horizon of frequency dynamics, H , into several segments, each with a time length $h_{\tau'}$, where τ' is the index. For each segment, we normalize the time range as $[0, 1]$. Using BP splines, we approximate $\Delta f(t)$ in each segment τ' as

$$\Delta f_{\tau'}(t) = (\Delta f_{\tau'}^B)^T B_3(t), \quad t \in [0, 1] \quad (18)$$

where Δf^B consists of the spline coefficients. PFR dynamics $P_g^{PR}(t)$ and $P_w^{PR}(t)$ are similarly handled and $P_g^{PR,B}$ and $P_w^{PR,B}$ are the corresponding spline coefficients.

Second, we integrate both sides of (2a) from 0 to t to yield

$$\int_0^t \left[\frac{2H_{\text{sys}}}{h_{\tau'}} \frac{d\Delta f(t)}{dt} + k_D P_d \Delta f(t) \right] dt = \int_0^t [\Delta P_d - \Delta P_{\text{sys}}^{PR}(t)] dt, \quad (19)$$

which by (17) is equivalent to

$$\frac{2H_{\text{sys}}}{h_{\tau'}} (\Delta f_{\tau'}^B - \Delta f_{\tau',ini}^B) + k_D P_d L^T \Delta f_{\tau'}^B = L^T (\Delta P_d^B - P_{\text{sys},\tau'}^{PR,B}) \quad (20a)$$

$$\Delta f_{\tau',ini}^{B,k} |_{\tau'=1} = \Delta f_{DB}, \quad \Delta f_{\tau',ini}^{B,k} |_{\tau'>1} = \Delta f_{\tau'-1}^{B,3}, \quad (20b)$$

where $\Delta f_{\tau',ini}^B$ is the initial value of $\Delta f_{\tau'}^B$ in period τ' and (20b) designates the initial condition for each period.

Similarly, (3) can be recast as

$$P_{\text{sys},\tau'}^{PR,B} = \sum_i (P_{g,i,\tau'}^{PR,B} + P_{w,i,\tau'}^{PR,B}) \quad (21a)$$

$$\frac{T_{g,i}}{h_{\tau'}} (P_{g,i,\tau'}^{PR,B} - P_{g,i,\tau',ini}^{PR,B}) + L^T P_{g,i,\tau'}^{PR,B} = G_{g,i} I_{g,i} L^T (\Delta f_{\tau'}^B - \Delta f_{DB}^B) \quad (21b)$$

$$P_{g,i,\tau',ini}^{PR,B,k} |_{\tau'=1} = 0, \quad P_{g,i,\tau',ini}^{PR,B,k} |_{\tau'>1} = P_{g,i,\tau'-1}^{PR,B,3} \quad (21c)$$

$$P_{w,i,\tau'}^{PR,B} = G_{w,i} (\Delta f_{\tau'}^B - \Delta f_{DB}^B), \quad (21d)$$

where $P_{w,i,\tau',ini}^{PR,B}$ is the initial value of $P_{w,i,\tau'}^{PR,B}$ in period τ' .

Finally, by (17e), constraints (4b) and (8c) are respectively implied by

$$J \Delta f_{\tau'}^B \leq \overline{\Delta f} \quad (22)$$

$$\text{and } \begin{cases} JP_{g,i,\tau,\tau'}^{PR,B} \leq R_{g,i,\tau}^{PR} \\ JP_{w,i,\tau,\tau'}^{PR,B} \leq R_{w,i,\tau}^{PR} \end{cases} \quad (23)$$

Consequently, we inner approximate the DAE frequency security constraints by general algebraic constraints (14), (15), and (20)–(23).

C. Linearization

We reformulate the bilinear terms $H_{\text{sys}}\Delta f_{\tau'}^B$ in (20a), $I_{g,i}\Delta f_{\tau'}^B$ in (21b), and $G_{w,i}\Delta f_{\tau'}^B$ in (21d) as linear forms for tractable computation. In what follows, we linearize $G_{w,i}\Delta f_{\tau'}^B$ as an example, and the linearization of other bilinear terms can be conducted similarly.

1) *Binary expansion*: Assuming that the droop factor G_w can only be adjusted discretely with a minimum stepsize ΔG_w [50], we encode G_w using binary decision variables ω_k as

$$G_w = \sum_{k=0}^{N_{BE}-1} \omega_k 2^k \Delta G_w, \quad \omega_k \in \{0, 1\}, \quad (24)$$

where N_{BE} is a pre-specified number for ω_k to adjust the granularity of the binary expansion.

2) *Big-M method*: With the above binary expansion, the bilinear term $G_w\Delta f_{\tau'}^B$ can be rewritten as $\Delta f_{\tau'}^B \sum_k \omega_k 2^k \Delta G_w$. Then, through the big-M method, the new bilinear terms $\alpha_{k,\tau'} = \omega_k \Delta f_{\tau'}^B$ can be linearized as

$$-M\omega_k \leq \alpha_{k,\tau'} \leq M\omega_k \quad (25a)$$

$$-M(1-\omega_k) + \Delta f_{\tau'}^B \leq \alpha_{k,\tau'} \leq \Delta f_{\tau'}^B + M(1-\omega_k). \quad (25b)$$

3) *DRCC Reformulation*: We follow [45] to recast the DRCC (12) as

$$P_{w,i,\tau} + R_{w,i,\tau}^{PR} \leq \mu_{i,\tau} - c_p \sigma_{i,\tau} \quad (26)$$

where c_p is a parameter that only depends on ε and r and can be computed beforehand.

We have recast the proposed frequency stability-constrained UC formulation (5)–(12) as a mixed-integer linear program, which can be directly computed by off-the-shelf solvers.

IV. CASE STUDY

We first demonstrate the tightness of the BP approximation. Then, using the IEEE 6-bus system, we analyze frequency security, influence of the dead band, variable droop factors, and parameter settings of the DRCCs. Finally, we demonstrate the scalability of our approach using an IEEE 118-bus system.

A. Tightness of Frequency Dynamics

We demonstrate the tightness of the BP approximation (20)–(21) in evaluating the nadir. We consider three thermal units and a wind farm and their parameters are the same as in the 6-bus system in Section IV-B (see Table V), except that for now we fix the droop factor of the wind farm at 20 MW/Hz. We illustrate the corresponding SFR model in Fig. 4, which is consistent with the frequency security constraints (1)–(3).

We consider a power imbalance of 20MW (about 10% of the total load) and the frequency dynamics in the subsequent horizon H . Fig. 5(a) depicts the frequency dynamics obtained from the BP approximation and those obtained from numerical

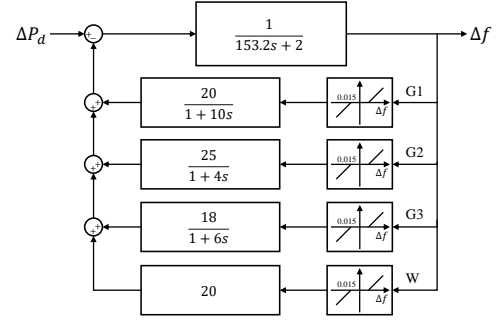
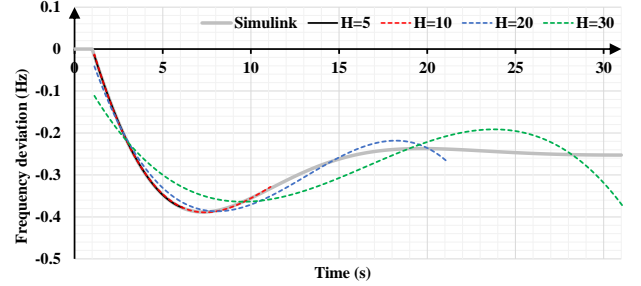
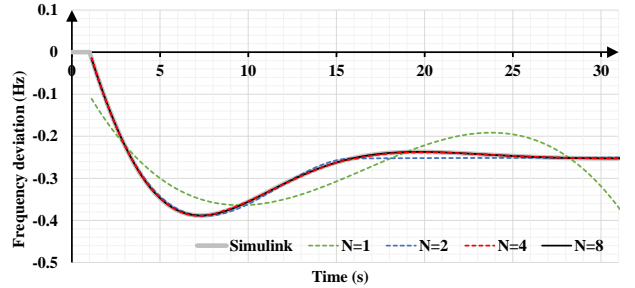


Fig. 4. SFR model with three thermal units and a wind farm



(a) Different lengths of horizon



(b) Different segment number

Fig. 5. Frequency dynamics from BP approximation vs. from Simulink

	Simulink	BP approximation			
		$H=5s$	$H=10s$	$H=20s$	$H=30s$
Nadir value (Hz)	-0.3884	-0.3778	-0.3892	-0.3866	-0.3759
Relative error	N/A	2.73%	0.20%	0.46%	3.21%

	Simulink	BP approximation			
		$N=1$	$N=2$	$N=4$	$N=8$
Nadir value (Hz)	-0.3884	-0.3759	-0.3893	-0.3892	-0.3883
Relative error	N/A	3.21%	0.23%	0.20%	0.02%

simulation (by Simulink). In this experiment, we vary the length of H from 5s to 30s and keep the segment number $N=1$. We report the estimated nadir values and their relative errors in Table II. From Fig. 5(a) and Table II, we observe that when $H=5s$, the BP approximation performs well in fitting frequency dynamics. However, in this case, $H=5s$ is too short for frequency dynamics to reach the nadir, which results in the 2.73% error. Instead, $H=10s$ is long enough

to reach the nadir, and hence, the relative error reduces to 0.20%. However, before an event occurs, system operators do not know when the nadir will take place and thus may select a relatively longer H to cover the nadir. In this case, as H gets longer, the relative error of nadir increases quickly. This is because the 1-segment BP approximation is not able to fit frequency dynamics for infinitely long. To tackle this issue, we divide H evenly into N segments and compare the results with different N . We use the 30s-horizon for analysis and report the obtained frequency dynamics and the estimated nadir values in Fig. 5(b) and Table III, respectively. Our results show that, as N increases, each segment shortens and the performance of BP quickly improves.

We provide a discussion on how to set up the BP approximation in a general condition. According to the above results, we notice that dividing the horizon H into multiple segments and applying a multi-segment BP approximation produce superb performance. On the other hand, in view of (20)–(23), the number of constraints in the corresponding UC formulation increases linearly with the number of segments. Consequently, we need to strike a right balance between approximation performance and computational burden. In addition, because the frequency nadir is the critical point of the dynamics, the BP segments before the nadir and covering the nadir is more important than those afterwards. Hence, we suggest an uneven division of H , in which the early segments should be shorter for a more accurate estimate of $\Delta f(t)|_{\text{nadir}}$ and the latter segments should be longer to relieve computational burden.

Along the above discussion, we divide the 30s-horizon into 4 segments with 10%, 20%, 30%, and 40% of the horizon, respectively. We depict the frequency dynamics approximation in this case in Fig. 6(a). From this figure, we observe that the BP approximation is highly accurate and the relative error in estimating $\Delta f(t)|_{\text{nadir}}$ is lower than 0.004%. In addition, we conduct an accuracy validation in the IEEE 118-bus system, and the system parameters will be given in Section IV.C. We show the results in Fig. 6(b). The BP approximation remains highly accurate in the 118-bus system and the relative error is lower than 0.12%. Moreover, if we set $H = 20\text{s}$, the relative error can be further reduced to lower than 0.03%. These results validate the tightness of the proposed method.

We also compare our BP approximation with the piecewise linearization used in [20]–[25]. Because the piecewise linearization method ignores the dead band and requires the response constant of all units to be the same, it is inapplicable to the case shown in Fig. 4. For comparison, we do not consider the dead band and modify all response constants to be 7s. We vary the total inertia H_{sys} and the sum of the droop factors of units G_g and obtain 99 evaluation points. 4 segments are considered for piecewise linearization. Fig. 7 compares the relative error of piecewise linearization and that of BP approximation in estimating nadir frequency deviation. TABLE IV provides the average relative error of the two methods. We can see that BP approximation performs better than piecewise linearization in most cases and the average relative error is one order of magnitude lower than that of piecewise linearization. The results validate the higher accuracy of BP approximation compared to existing methods.

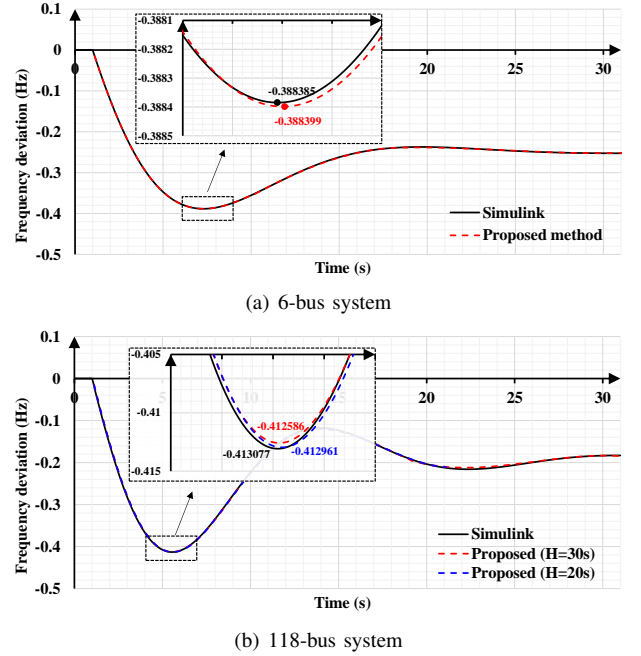


Fig. 6. BP approximation with an uneven division of the horizon

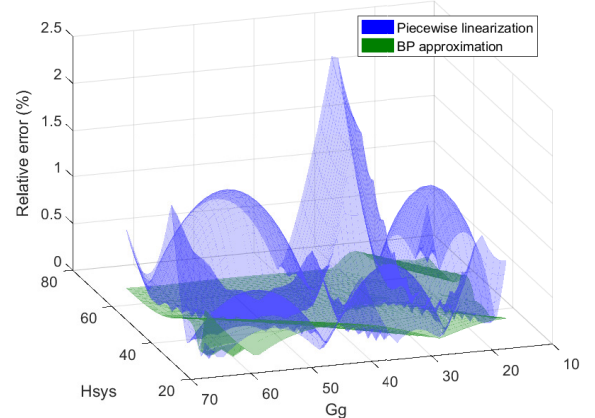


Fig. 7. Relative error in estimating Δf_{nadir}

TABLE IV
AVERAGE RELATIVE ERRORS IN ESTIMATING Δf_{NADIR}

	Piecewise Linearization	BP approximation
Average relative error	0.5031%	0.0653%
Highest relative error	2.2734%	0.5543%

B. 6-Bus System

Next, we use the IEEE 6-bus system for analysis. The system includes 3 thermal units (G1, G2, and G3) and a newly-added wind farm (W). The load curve and the predicted available wind power are depicted in Fig. 8. The maximum total load is 210MW. The standard deviation of wind power prediction is set as 5% of the predicted value. The risk level ε in chance constraints is set as 10% and the radius r of the Wasserstein ball for DRCC is set as 0.01.

Table V displays the main technical parameters of thermal units and the wind farm. The fuel cost coefficients are the same as in [54]. The droop factor of the wind farm is set as 20 MW/Hz by default and can be adjusted from 10 MW/Hz to 25

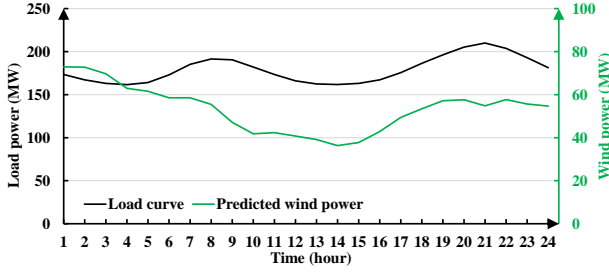


Fig. 8. Load curve and predicted wind power

Units	G1	G2	G3	W
Capacity (MW)	200	150	180	80
Minimum generation (MW)	60	45	54	N/A
Inertia constant (s)	8	5	6	5
Response constant (s)	10	4	6	0
Droop factor (MW/Hz)	20	25	18	10~25

MW/Hz with a stepsize of 5 MW/Hz. The nominal frequency is 50 Hz and the dead band is set as 0.015 Hz [30]. The cost coefficients of PFR reserves are 15 \$/MWh and 5 \$/MWh for thermal units and the wind farm, respectively. In each hour, we consider a sudden power imbalance of 10% total load [7]. We set the load damping factor as 1% total load per Hz, the maximum admitted RoCoF as 0.5 Hz/s, and the maximum admitted frequency deviation at the nadir and at the QSS as 0.5 Hz and 0.3 Hz, respectively [21]. We consider a 30s-horizon of frequency dynamics and divide it into 4 segments with 10%, 20%, 30%, and 40% of the horizon, respectively.

1) *Baseline Results:* With the above parameter settings, we compare the following two UC formulations:

(Case 1) without frequency security constraints; and

(Case 2) with frequency security constraints (4) and (8).

Note that in Case 1, we do not consider frequency security constraints but require the total PFR reserve to be no less than the set power imbalance. We report the optimal UC solutions and frequency security metrics of these two cases in Figs. 9 and 10, respectively, as well as their performance details in Table VI.

From Fig. 9 and Table VI, we observe that in Case 1, only G1 is online. For this case, we simulate the frequency dynamics under power imbalance and find that in hour 21, the frequency deviation reaches 0.7133 Hz at the nadir and reaches 0.5131 Hz at the QSS, which exceeds the frequency security limits (by 0.5 Hz and 0.3 Hz, respectively). The frequency dynamics of hour 21 in Case 1 are provided in Fig. 11.

In contrast, in Case 2, G1 and G2 are always online and G3 is started up in hour 21, which provides more inertia and PFR capacity than those in Case 1. We depict the PFR reserve and the droop factor of the wind farm in Fig. 12. From this figure, we observe that most wind power is integrated for power supply or reserved for frequency support, and a only small portion of wind power is curtailed in the last two hours. In addition, the droop factor varies across different hours, which will be further discussed later. As a consequence of more units online and more PFR reserves from both the thermal

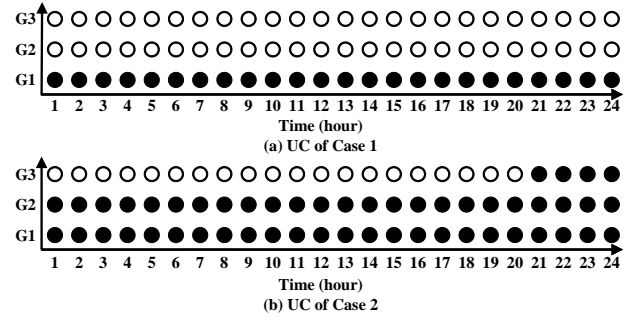


Fig. 9. Optimal UC in Cases 1 and 2

Comparison terms	Case 1	Case 2
Start-up & shut-down cost (\$)	0	5400
Fuel cost of thermal units (\$)	43763.09	49040.87
PFR reserve cost of thermal units (\$)	6445.92	5171.99
PFR reserve cost of wind farm (\$)	0	919.69
Total cost (\$)	50209.01	60532.55
Total PFR reserve of thermal units (MWh)	429.73	344.80
Total PFR reserve of wind farm (MWh)	0	183.94
Maximum RoCoF (Hz/s)	0.2625	0.1866
Maximum Δf at the nadir (Hz)	0.7133	0.4578
Maximum Δf at the quasi-steady state (Hz)	0.5131	0.2995
Computation time (s)	8.61	38.42

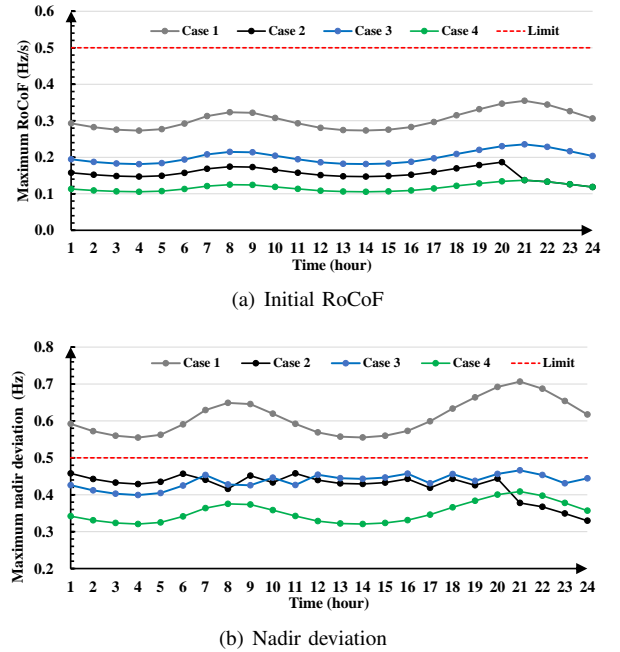


Fig. 10. Initial RoCoF and nadir deviation at different periods

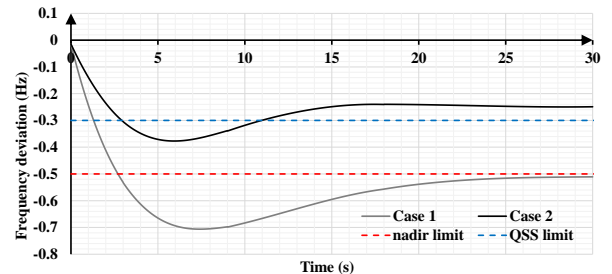


Fig. 11. Frequency dynamics of hour 21 in Cases 1 and 2

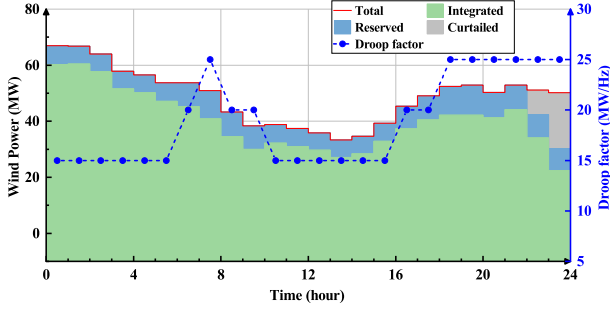


Fig. 12. Operation of the wind farm in Case 2

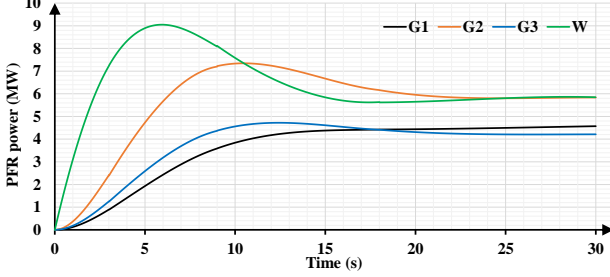


Fig. 13. PFR power dynamics of hour 21 in Case 2

units and the wind farm, in Case 2, the maximum frequency deviation becomes 0.4578 Hz at the nadir and 0.2995 Hz at the QSS, significantly lower than those in Case 1. Note that, since G3 is online from hour 21 in Case 2, the maximum nadir frequency deviation occurs in hour 20 and the maximum QSS frequency deviation occurs in hour 11. We also depict the frequency dynamics of hour 21 in Case 2 in Fig. 11 for comparison and the corresponding PFR power dynamics in Fig. 13. Because the unit commitment is discrete and the status change of any unit will strongly affect frequency dynamics, it is hard to find a unit commitment that is just right to satisfy all frequency security limits, for which the frequency dynamics of Case 2 in Fig. 11 seem conservative. The above analyses demonstrate that the proposed model can effectively protect frequency security.

2) *Impact of the Dead Band*: To evaluate the value of modeling the dead band in frequency security, we consider a third UC formulation: (Case 3) without considering the dead band in Case 2.

We report the optimal UC solution in Case 3 in Fig. 14 and the performance details in Table VII. From Fig. 14 and Table VII, we observe that in Case 3, G2 and G3 remain online while G1 remains offline across all periods. Because the more economic G2 and G3 are utilized, the total cost in Case 3 is lower than that in Case 2. However, ignoring the dead band causes undesirable frequency dynamics. From Table VII, we observe that the maximum $\Delta f(t)|_{\text{QSS}}$ in Case 3 reaches 0.3141 Hz, exceeding frequency security limit (0.3 Hz). This highlights the necessity of considering the dead band in frequency stability-constrained UC.

3) *Benefits of Variable Droop Factors*: To evaluate the benefit of adopting variable droop factors of the wind farm, as opposed of constant droop factors, we consider a fourth UC formulation:

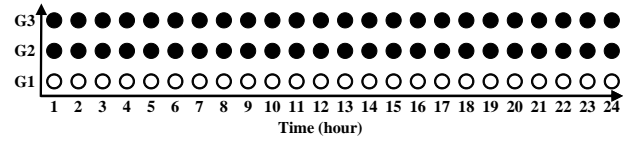


Fig. 14. Optimal UC in Case 3

TABLE VII
DETAILED COMPARISON BETWEEN CASES 3 AND 2

Comparison terms	Case 3	Case 2
Start-up & shut-down cost (\$)	0	5400
Fuel cost of thermal units (\$)	47718.70	49040.87
PFR reserve cost of thermal units (\$)	4712.09	5171.99
PFR reserve cost of wind farm (\$)	1033.06	919.69
Total cost (\$)	53463.85	60532.55
Maximum RoCoF (Hz/s)	0.2354	0.1866
Maximum Δf at the nadir (Hz)	0.4662	0.4578
Maximum Δf at the quasi-steady state (Hz)	0.3141	0.2995
Computation time (s)	57.15	38.42

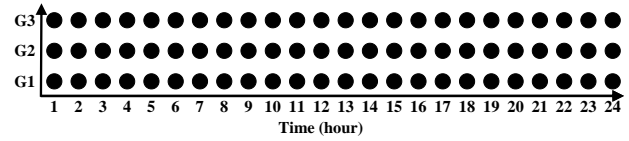


Fig. 15. Optimal UC in Case 4

TABLE VIII
DETAILED COMPARISON BETWEEN CASES 4 AND 2

Comparison terms	Case 4	Case 2
Start-up & shut-down cost (\$)	0	5400
Fuel cost of thermal units (\$)	59198.07	49040.87
PFR reserve cost of thermal units (\$)	5595.82	5171.99
PFR reserve cost of wind farm (\$)	809.83	919.69
Total cost (\$)	65603.72	60532.55
Maximum RoCoF (Hz/s)	0.1371	0.1866
Maximum Δf at the nadir (Hz)	0.4087	0.4578
Maximum Δf at the quasi-steady state (Hz)	0.2614	0.2995
Computation time (s)	4.89	38.42

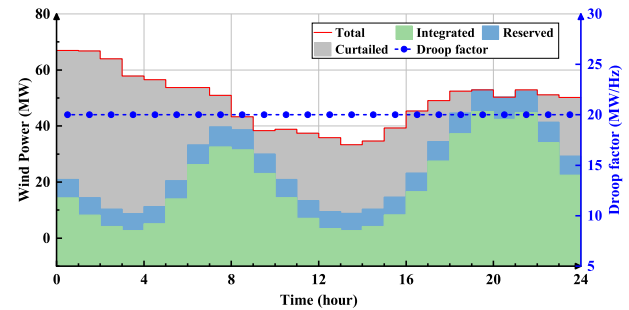


Fig. 16. Operation of the wind farm in Case 4

(Case 4) fixing the droop factor in Case 2 at 20 MW/Hz.

We report the optimal UC solution in Case 4 in Fig. 15 and the performance details in Table VIII.

From Fig. 15 and Table VIII, we observe that in Case 4, all thermal units remain online all the time and the total cost is higher than that in Case 2. We provide the PFR reserve and droop factors of the wind farm in Case 4 in Fig. 16. Comparing Figs. 16 and 12, we observe that much more wind

curtailment occurs in Case 4. The reason is analyzed in the following. In Case 4, if we replace its UC with that in Case 2 while keeping the droop factors unchanged, $\Delta f(t)|_{QSS}$ would reach 0.3007 Hz at hour 8 and 0.3207 Hz at hour 20, which exceed the frequency security limit (0.3 Hz). Hence, in Case 4, G3 needs to be online to reduce $\Delta f(t)|_{QSS}$, and consequently, much wind power needs to be curtailed to satisfy the minimum generation limits of the thermal units. In contrast, in Case 2, we reduce $\Delta f(t)|_{QSS}$ by increasing the droop factor (such as in hours 8 and 20; see Fig. 12), which avoids putting G3 online and reduces the total cost by 7.69%. These results demonstrate that variable droop factors can improve the coordination of different frequency resources for higher operation economy.

4) *Comparison with Existing Methods*: To compare our method with the piecewise linearization method in existing works [20]–[25], we consider a fifth UC formulation:

(Case 5) replacing BP approximation in Case 3 by piecewise linearization.

There are some notes for the comparison. First, due to the assumptions of the piecewise linearization method, we do not consider the dead band and modify all response constants to be 7s. Accordingly, we compare Case 5 with Case 3. Second, since it is hard to derive an accurate piecewise linearization, to relieve the computational burden, we only use the possible combinations of UC and G_w as evaluate points. Deriving the linearization consumes about 600s. Third, the piecewise linearization method does not calculate the maximum PFR power during frequency dynamics, so we choose a conservative PFR reserve according to droop factors and Δf_{err} .

We report the performance details in TABLE IX, and the optimal UC in Case 5 is the same as in Fig. 14. We can see that the total cost of Case 5 is higher than that of Case 3, mainly due to the conservative PFR reserve of units. The computational time of Case 5 is much less than that of Case 3, because the piecewise linearization method induces a more tractable nadir constraint. With the solution of Case 5, we compare the exact nadir deviation and the estimated nadir deviation of piecewise linearization and BP approximation in each period, and the results are shown in Fig. 17. We observe that BP approximation has higher accuracy in estimating nadir deviation. In addition, piecewise linearization usually provides a lower estimation than the exact value of the nadir deviation (see Fig. 17), which is optimistic and may cause security risks.

5) *Analysis on DRCCs*: We first compare the deterministic approach and the adopted DRCC approach (Case 2). The deterministic approach gives the same UC solution as in Case 2 and incurs a lower operation cost. Nevertheless, the DRCC approach explicitly considers the possibility of having less wind power available than predicted and allocates more generation and reserves on the thermal units, which helps reduce the re-dispatch of thermal units [49]. The re-dispatch cost coefficient is set as 40\$/MWh and 1000 scenarios are randomly generated. So the expected re-dispatch costs of the deterministic approach and the DRCC approach are 819.01\$ and 45.76\$, respectively. The latter is far less than the former, which validates the effectiveness of DRCC in reducing risks.

Next, we vary the risk level ϵ and the Wasserstein ball radius r to see their impacts on the total cost of the UC

TABLE IX
DETAILED COMPARISON BETWEEN CASES 3 AND 5

Comparison terms	Case 3	Case 5
Start-up & shut-down cost (\$)	0	0
Fuel cost of thermal units (\$)	47718.70	47878.25
PFR reserve cost of thermal units (\$)	4712.09	7740
PFR reserve cost of wind farm (\$)	1033.06	1100
Total cost (\$)	53463.85	56718.25
Maximum RoCoF (Hz/s)	0.2354	0.2354
Maximum Δf at the nadir (Hz)	0.4518	0.4959
Maximum Δf at the quasi-steady state (Hz)	0.2996	0.2996
Computation time (s)	57.15	14.20

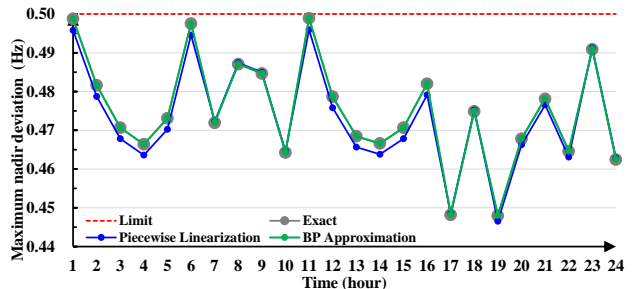
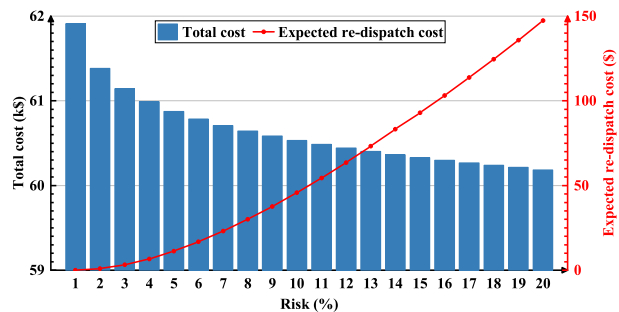
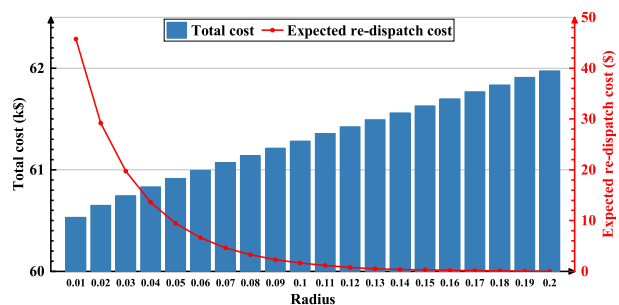


Fig. 17. Nadir frequency deviation in Case 5



(a) Risk level ϵ



(b) Radius r of the Wasserstein ball

Fig. 18. DRCC sensitivity analysis

model and the expected re-dispatch cost. The results are reported in Fig. 18. This figure provides clear trade-offs among operational economy, risk attitude, and robustness, which can better assist the system operators. In particular, the total cost is more sensitive to the risk level than it is to the Wasserstein ball radius, especially when ϵ is small (or equivalently, when $1 - \epsilon$ is close to 1). When ϵ exceeds 0.1, the sensitivity of the total cost to ϵ and r are similar.

C. Scalability Test in IEEE 118-Bus System

We evaluate the scalability of our approach using the IEEE 118-bus system, which includes 54 thermal units and a 4242 MW of maximum total load. We follow [30] on the frequency-related parameters. We scale up the capacity of the wind farm to 800 MW and accordingly the wind power and the range of the droop factors. The results are reported in Table X.

TABLE X
RESULTS IN IEEE 118-BUS SYSTEM

Comparison terms	Case 1	Case 2
Operation cost of thermal units (k\$)	2184.18	2394.85
PFR reserve cost of thermal units (k\$)	130.21	155.65
PFR reserve cost of wind farm (k\$)	0	9.81
Total cost (k\$)	2314.39	2560.31
Maximum RoCoF (Hz/s)	0.2598	0.1696
Maximum Δf at the nadir (Hz)	0.7748	0.4318
Maximum Δf at the quasi-steady state (Hz)	0.4950	0.1935
Computation time (s)	49.98	2472

From Table X, we observe that in Case 1, the frequency deviation of hour 21 reaches 0.7748 Hz at the nadir and reaches 0.4950 Hz at the QSS, exceeding the frequency security limits. In contrast, in Case 2, all frequency security limits are respected. (see Fig. 19). Nevertheless, the computational time in Case 2 is much longer than that in Case 1, which can be seen as the cost of guaranteeing frequency security. It is hence interesting to further improve the computational tractability of the proposed method and investigate the right trade-off between its performance and computational burden in future study. Fig. 20 provides the PFR power in Case 2. These results demonstrate the effectiveness and scalability of the proposed method in protecting frequency security in larger-sized systems.

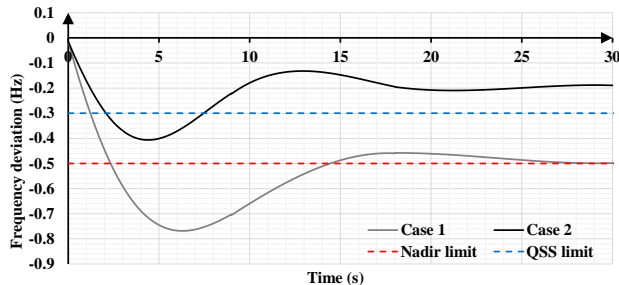


Fig. 19. Comparison of frequency dynamics in IEEE 118-bus system

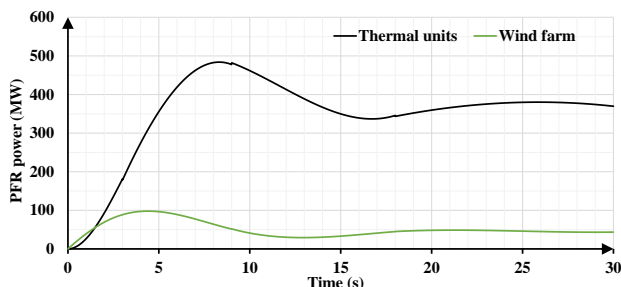


Fig. 20. PFR power dynamics of Case 2 in IEEE 118-bus system

V. CONCLUSIONS

This paper proposed a frequency stability-constrained UC model considering frequency dynamics, wind power uncertainty, and variable droop factors. In this model, we incorporated frequency dynamics using DAEs and considered the dead band. Then, we derived an inner approximation of the DAEs using BP splines and linearization techniques. A comparison with Simulink demonstrated the tightness of the BP approximation in depicting frequency dynamics and evaluating the frequency deviation at the nadir. Extensive case studies based on IEEE 6-bus and 118-bus systems demonstrated the effectiveness of the proposed model in deciding UC and PFR reserves for frequency security, the necessity of considering the dead band in frequency dynamics, and the value of using variable droop factors of the wind farms in improving the coordination among different frequency support resources, which can help reduce the total cost significantly. Future works will consider more types of frequency response resources, such as energy storage, to support frequency stability in a market environment.

REFERENCES

- [1] IRENA, "Renewable energy statistics 2021," International Renewable Energy Agency, Tech. Rep., 2021.
- [2] L. Xie, P. M. S. Carvalho, L. A. F. M. Ferreira, J. Liu, B. H. Krogh, N. Popli, and M. D. Ilic, "Wind integration in power systems: Operational challenges and possible solutions," *Proceedings of the IEEE*, vol. 99, no. 1, pp. 214–232, 2011.
- [3] H. D. Tafti, Q. Wang, C. D. Townsend, J. Pou, and G. Konstantinou, "Global flexible power point tracking in photovoltaic systems under partial shading conditions," *IEEE Transactions on Power Electronics*, vol. 37, no. 9, pp. 11 332–11 341, 2022.
- [4] H. Abiari, T. Daemi, and S. A. Saeid, "Frequency-constrained unit commitment under uncertain PFR of energy storage systems," *Journal of Energy Storage*, vol. 73, p. 108848, 2023.
- [5] J. Zhu, C. D. Booth, G. P. Adam, A. J. Roscoe, and C. G. Bright, "Inertia emulation control strategy for VSC-HVDC transmission systems," *IEEE Transactions on Power Systems*, vol. 28, no. 2, 2013.
- [6] S. Saberi Oskouee, S. Kamali, and T. Amraee, "Primary frequency support in unit commitment using a multi-area frequency model with flywheel energy storage," *IEEE Transactions on Power Systems*, vol. 36, no. 6, pp. 5105–5119, 2021.
- [7] Y. Wen, W. Li, G. Huang, and X. Liu, "Frequency dynamics constrained unit commitment with battery energy storage," *IEEE Transactions on Power Systems*, vol. 31, no. 6, pp. 5115–5125, 2016.
- [8] J. Rocabert, A. Luna, F. Blaabjerg, and P. R. Iiguez, "Control of power converters in ac microgrids," *IEEE Transactions on Power Electronics*, vol. 27, no. 11, pp. 4734–4749, 2012.
- [9] H. Dehghani Tafti, G. Konstantinou, J. Fletcher, L. Callegaro, G. Farivar, and J. Pou, "Control of distributed photovoltaic inverters for frequency support and system recovery," *IEEE Transactions on Power Electronics*, vol. 37, no. 4, pp. 4742–4750, 2022.
- [10] J. F. Restrepo and F. D. Galiana, "Unit commitment with primary frequency regulation constraints," *IEEE Transactions on Power Systems*, vol. 20, no. 4, pp. 1836–1842, 2005.
- [11] H. Golpira, S. Amini, A. Atarodi, and H. Bevrani, "A data-driven inertia adequacy-based approach for sustainable expansion planning in distributed generations-penetrated power grids," *IET Generation Transmission & Distribution*, vol. 16, no. 22, pp. 4614–4629, 2022.
- [12] F. D. Galiana, F. Bouffard, J. M. Arroyo, and J. F. Restrepo, "Scheduling and pricing of coupled energy and primary, secondary, and tertiary reserves," *Proceedings of the IEEE*, vol. 93, no. 11, pp. 1970–1983, 2005.
- [13] K. V. Vidyandandan and N. Senroy, "Primary frequency regulation by deloaded wind turbines using variable droop," *IEEE Transactions on Power Systems*, vol. 28, no. 2, pp. 837–846, 2013.
- [14] Y.-Y. Lee and R. Baldick, "A frequency-constrained stochastic economic dispatch model," *IEEE Transactions on Power Systems*, vol. 28, no. 3, pp. 2301–2312, 2013.

- [15] L. Badesa, F. Teng, and G. Strbac, "Simultaneous scheduling of multiple frequency services in stochastic unit commitment," *IEEE Transactions on Power Systems*, vol. 34, no. 5, pp. 3858–3868, 2019.
- [16] K. Li, H. Guo, X. Fang, S. Liu, F. Teng, and Q. Chen, "Market mechanism design of inertia and primary frequency response with consideration of energy market," *IEEE Transactions on Power Systems*, vol. 38, no. 06, pp. 5701–5713, 2023.
- [17] L. Badesa, F. Teng, and G. Strbac, "Conditions for regional frequency stability in power system scheduling-part I: Theory," *IEEE Transactions on Power Systems*, vol. 36, no. 6, pp. 5558–5566, 2021.
- [18] X. Zhao, H. Wei, J. Qi, P. Li, and X. Bai, "Frequency stability constrained optimal power flow incorporating differential algebraic equations of governor dynamics," *IEEE Transactions on Power Systems*, vol. 36, no. 3, pp. 1666–1676, 2021.
- [19] M. Liu, F. Bizzarri, A. M. Brambilla, and F. Milano, "On the impact of the dead-band of power system stabilizers and frequency regulation on power system stability," *IEEE Transactions on Power Systems*, vol. 34, no. 5, pp. 3977–3979, 2019.
- [20] Z. Zhang, M. Zhou, Z. Wu, S. Liu, Z. Guo, and G. Li, "A frequency security constrained scheduling approach considering wind farm providing frequency support and reserve," *IEEE Transactions on Sustainable Energy*, vol. 13, no. 2, pp. 1086–1100, 2022.
- [21] H. Li, Y. Qiao, Z. Lu, B. Zhang, and F. Teng, "Frequency-constrained stochastic planning towards a high renewable target considering frequency response support from wind power," *IEEE Transactions on Power Systems*, vol. 36, no. 5, pp. 4632–4644, 2021.
- [22] H. Ahmadi and H. Ghasemi, "Security-constrained unit commitment with linearized system frequency limit constraints," *IEEE Transactions on Power Systems*, vol. 29, no. 4, pp. 1536–1545, 2014.
- [23] Z. Zhang, E. Du, F. Teng, N. Zhang, and C. Kang, "Modeling frequency dynamics in unit commitment with a high share of renewable energy," *IEEE Transactions on Power Systems*, vol. 35, no. 6, pp. 4383–4395, 2020.
- [24] L. Liu, Z. Hu, Y. Wen, and Y. Ma, "Modeling of frequency security constraints and quantification of frequency control reserve capacities for unit commitment," *IEEE Transactions on Power Systems*, pp. 1–12, 2023.
- [25] Y. Zhang, S. Wu, J. Lin, Q. Wu, C. Shen, and F. Liu, "Frequency reserve allocation of large-scale RES considering decision-dependent uncertainties," *IEEE Transactions on Sustainable Energy*, pp. 1–15, 2023.
- [26] M. Paturet, U. Markovic, S. Delikaraoglu, E. Vrettos, P. Aristedou, and G. Hug, "Stochastic unit commitment in low-inertia grids," *IEEE Transactions on Power Systems*, vol. 35, no. 3, pp. 3448–3458, 2020.
- [27] Y. Shen, W. Wu, B. Wang, and S. Sun, "Optimal allocation of virtual inertia and droop control for renewable energy in stochastic look-ahead power dispatch," *IEEE Transactions on Sustainable Energy*, vol. 14, no. 3, pp. 1881–1894, 2023.
- [28] M. Javadi, T. Amraee, and F. Capitanescu, "Look ahead dynamic security-constrained economic dispatch considering frequency stability and smart loads," *International Journal of Electrical Power & Energy Systems*, vol. 108, pp. 240–251, 2019.
- [29] M. Javadi, Y. Gong, and C. Y. Chung, "Frequency stability constrained bess sizing model for microgrids," *IEEE Transactions on Power Systems*, pp. 1–13, 2023.
- [30] L. Yang, Y. Xu, J. Zhou, and H. Sun, "Distributionally robust frequency constrained scheduling for an integrated electricity-gas system," *IEEE Transactions on Smart Grid*, vol. 13, no. 4, pp. 2730–2743, 2022.
- [31] Z. Chu, N. Zhang, and F. Teng, "Frequency-constrained resilient scheduling of microgrid: A distributionally robust approach," *IEEE Transactions on Smart Grid*, vol. 12, no. 6, pp. 4914–4925, 2021.
- [32] Y. Yang, J. C.-H. Peng, C. Ye, Z.-S. Ye, and Y. Ding, "A criterion and stochastic unit commitment towards frequency resilience of power systems," *IEEE Transactions on Power Systems*, vol. 37, no. 1, pp. 640–652, 2022.
- [33] K. Li, X. Ai, J. Fang, S. Cui, Y. Feng, D. Liu, P. Gu, W. Qiu, and J. Wen, "Frequency security constrained robust unit commitment for sufficient deployment of diversified frequency support resources," *IEEE Transactions on Industry Applications*, pp. 1–12, 2023.
- [34] L. Badesa, F. Teng, and G. Strbac, "Optimal portfolio of distinct frequency response services in low-inertia systems," *IEEE Transactions on Power Systems*, vol. 35, no. 6, pp. 4459–4469, 2020.
- [35] V. Trovato, "System scheduling with optimal time-varying delivery intervals for frequency response," *IEEE Transactions on Power Systems*, vol. 37, no. 6, pp. 1–1, 2022.
- [36] Y. Zhang, H. Cui, J. Liu, F. Qiu, T. Hong, R. Yao, and F. Li, "Encoding frequency constraints in preventive unit commitment using deep learning with region-of-interest active sampling," *IEEE Transactions on Power Systems*, vol. 37, no. 3, pp. 1942–1955, 2022.
- [37] L. Sang, Y. Xu, Z. Yi, L. Yang, H. Long, and H. Sun, "Conservative sparse neural network embedded frequency-constrained unit commitment with distributed energy resources," *IEEE Transactions on Sustainable Energy*, vol. 14, no. 04, pp. 2351–2363, 2023.
- [38] R. Jiang, J. Wang, and Y. Guan, "Robust unit commitment with wind power and pumped storage hydro," *IEEE Transactions on Power Systems*, vol. 27, no. 2, pp. 800–810, 2012.
- [39] T. Ding, Z. Zeng, M. Qu, J. P. S. Catalao, and M. Shahidepour, "Two-stage chance-constrained stochastic thermal unit commitment for optimal provision of virtual inertia in wind-storage systems," *IEEE Transactions on Power Systems*, vol. 36, no. 4, pp. 3520–3530, 2021.
- [40] S. Zheng, K. Liao, J. Yang, and Z. He, "Optimal scheduling of distribution network with autonomous microgrids: Frequency security constraints and uncertainties," *IEEE Transactions on Sustainable Energy*, vol. 14, no. 01, pp. 613–629, 2023.
- [41] Y. Zhang, S. Shen, and J. Mathieu, "Distributionally robust chance-constrained optimal power flow with uncertain renewables and uncertain reserves provided by loads," *IEEE Transactions on Power Systems*, vol. 32, no. 2, pp. 1378–1388, 2017.
- [42] L. Jiang, Z. Bie, T. Long, X. Wang, H. Xie, and G. Li, "A post-event generator start-up strategy for renewable penetrated transmission system considering dynamic frequency regulation," *IEEE Transactions on Sustainable Energy*, vol. 14, no. 02, pp. 1135–1150, 2023.
- [43] B. Zhou, J. Fang, X. Ai, C. Yang, W. Yao, and J. Wen, "Dynamic Var reserve-constrained coordinated scheduling of LCC-HVDC receiving-end system considering contingencies and wind uncertainties," *IEEE Transactions on Sustainable Energy*, vol. 12, no. 1, pp. 469–481, 2021.
- [44] B. Li, R. Jiang, and J. L. Mathieu, "Ambiguous risk constraints with moment and unimodality information," *Mathematical Programming*, vol. 173, no. 1, pp. 151–192, 2019.
- [45] H. Shen and R. Jiang, "Chance-constrained set covering with Wasserstein ambiguity," *Mathematical programming*, vol. 198, no. 1, pp. 621–674, 2023.
- [46] —, "Wasserstein two-sided chance constraints with an application to optimal power flow," *arXiv preprint arXiv:2204.00191*, 2022.
- [47] Y. Yuan, Y. Zhang, J. Wang, Z. Liu, and Z. Chen, "Enhanced frequency-constrained unit commitment considering variable-droop frequency control from converter-based generator," *IEEE Transactions on Power Systems*, vol. 38, no. 02, pp. 1094–1110, 2023.
- [48] M. Parvania and A. Scaglione, "Unit commitment with continuous-time generation and ramping trajectory models," *IEEE Transactions on Power Systems*, vol. 31, no. 4, pp. 3169–3178, 2016.
- [49] B. Zhou, J. Fang, X. Ai, W. Yao, and J. Wen, "Flexibility-enhanced continuous-time scheduling of power system under wind uncertainties," *IEEE Transactions on Sustainable Energy*, vol. 12, no. 4, pp. 2306–2320, 2021.
- [50] B. Zhou, J. Fang, X. Ai, S. Cui, W. Yao, Z. Chen, and J. Wen, "Storage right-based hybrid discrete-time and continuous-time flexibility trading between energy storage station and renewable power plants," *IEEE Transactions on Sustainable Energy*, vol. 14, no. 01, pp. 465–481, 2023.
- [51] C. Zheng, J. Fang, S. Wang, X. Ai, Z. Liu, and Z. Chen, "Energy flow optimization of integrated gas and power systems in continuous time and space," *IEEE Transactions on Smart Grid*, vol. 12, no. 3, pp. 2611–2624, 2021.
- [52] M. F. M. Arani and E. F. El-Saadany, "Implementing virtual inertia in DFIG-based wind power generation," *IEEE Transactions on Power Systems*, vol. 28, no. 2, pp. 1373–1384, 2013.
- [53] J. Fang, H. Li, Y. Tang, and F. Blaabjerg, "Distributed power system virtual inertia implemented by grid-connected power converters," *IEEE Transactions on Power Electronics*, vol. 33, no. 10, pp. 8488–8499, 2018.
- [54] B. Zhou, J. Fang, X. Ai, Y. Zhang, W. Yao, Z. Chen, and J. Wen, "Partial-dimensional correlation-aided convex-hull uncertainty set for robust unit commitment," *IEEE Transactions on Power Systems*, vol. 38, no. 03, pp. 2434–2446, 2023.